Corrosion Science 194 (2022) 109920

Contents lists available at ScienceDirect

Corrosion Science

journal homepage: www.elsevier.com/locate/corsci

The effect of Mo and Ge reactive elements on high-temperature oxidation of higher manganese silicide

Antoine de Padoue Shyikira [a,*], Naureen Akhtar [a], Gunstein Skomedal [a,b], Peter Hugh Middleton [a]

[a] University of Agder, Norway
[b] Elkem ASA-Kristiansand, Norway

ARTICLE INFO

Keywords:
Higher manganese silicides
High-temperature corrosion
Thermal oxidation
Silicide thermoelectric materials

ABSTRACT

Higher manganese silicide (HMS) alloys ($Mn_{x-\alpha}Mo_{\alpha}Si_{y-\beta}Ge_{\beta}$ (x = 0.99–1.011, α = 0.005–0.02, y = 1.75, β = 0.005–0.01)) were studied to elucidate the effect of Mo and Ge pertaining to oxidation. Oxidation experiments were conducted using thermogravimetry and characterized using x-ray photoelectron spectroscopy (XPS) and scanning electron microscopy (SEM). Isoconversion experiments below 450 °C, shows that doping (up to 2 at%) raises the oxidation potential of HMS. Isothermally, the oxidation rate reduces buy one order of magnitude by doping on Mn and/or Si sites from 0.5 to 2 at%, revealing that the dopants-based oxides do not lessen the robustness of SiO_2 oxide.

1. Introduction

Thermal oxidation robustness in thermoelectricity is an important facet to consider while studying the stability of thermoelectric materials and modules. D.P. Whittle and J. Stringer [1] defines two essential requirements for alloys to withstand thermal oxidation, first to grow an oxide that thickens at a slow rate, and second that the oxide adheres to the alloy surface at any condition (thermal or environmental). Similarly, higher manganese silicide (HMS) as a binary alloy oxidises selectively forming a stable and protective silicon dioxide (SiO_2). As discussed in our recent publication [2], oxidation stability concerns stem from the level of impurities/dopants and the synthesis route including densification. In this article, much focus is put on the effect of dopants, and doping sites in the HMS matrix.

The benefits of "Al" and "Ge" doping on HMS were observed in our recent article [2], and thoroughly reviewed by Y. Miyazaki [3]. The common interest with HMS doping as a semiconductor is improved electrical conductivity of the thermoelectric (TE) materials, through increased charge carrier concentration. Moreover, particularly with Ge doping on the Si-site, a considerable reduction of MnSi striation was reported [4,5], the latter being another factor that lowers the electrical conductivity of the materials due to lack of crystallographic relationship between HMS and MnSi polycrystalline phases [6]. A similar effect (reduced striation) was also reported in case of doping on the Mn-site with Cr and Co ([7,8] and [9], respectively).

The effect of doping on the oxidation of alloys has been investigated on several compounds or systems, mostly on alumina and chromia scale adhesion [1,10–12], though not much was done on HMS. The main outcome of the studies was that the reactive elements (RE) additives, improved the oxide scale adhesion, interfacial diffusion, mechanical and chemical potential in the alloys or oxide scales. However, D. Naumenko et.al. [11], showed that another important aspect to consider is the level of interactions between RE and other elemental constituents of the alloy, since these reactions may complicate the optimisation of RE-dopant type and content.

The current study is a continuation of [2], we empirically discuss the oxidation kinetics/mechanisms of HMS (and its alloys), and qualitatively present the effect of dopant on the oxidation of HMS. A deviation in the oxidation kinetics of the pure HMS due to dopants and a thorough discussion of the mechanism is reported in this article. Finally, the coexistence of resultant Mo- and Ge-oxide species with the protective SiO_2 is presented, and an outlook towards further improvement is provided.

* Corresponding author.
E-mail addresses: antoine.d.shyikira@uia.no, tonnydepadoue15@gmail.com (A. de Padoue Shyikira).

https://doi.org/10.1016/j.corsci.2021.109920
Received 6 September 2021; Received in revised form 26 October 2021; Accepted 26 October 2021
Available online 31 October 2021

Table 1
Elemental composition by EDS of alloys in Fig. 1.

Alloy	Spot	Si [at %]	Mn [at %]	Ge [at %]	Mo [at %]	Tentative phases
$Mn_{0.97}Mo_{0.02}Si_{1.75}$	1	62	38			$MnSi_{1.75}$
	2	64	36			$MnSi_{1.75}$
	3	52	47		1	MnSi
	4	51	48		1	MnSi
	5	65	12		23	Mo rich
	6	66	13		21	Mo rich
$Mn_{0.99}Mo_{0.02}Si_{1.73}Ge_{0.02}$	1	63	37			$MnSi_{1.75}$
	2	64	13		23	Mo rich
	3	50	50			MnSi
	4	54	19	22		Ge rich

2. Materials and methods

2.1. Powder and pellet production

HMS alloys $Mn_{x-\alpha}$ Mo_{α} $Si_{y-\beta}$ Ge_{β} (x = 0.99–1.011, α = 0.005 – 0.02, y = 1.75, β = 0.005 – 0.01) were synthesized (check Table 2), an overview of raw material type and composition can be found in Table 1 of reference [2]. The elemental powder of Mn and Si were pre-alloyed with Mo and Ge, respectively. The pre-alloyed mixtures (Mn-Mo and/or Si-Ge) were mixed in a lid covered graphite crucible and heated fast (heating rate 100 °C/min) up to 1400 °C backfilling with Argon. The process was held for 10 min and then further heated up to above silicon melting temperature (specifically at 1450 °C). This temperature was then held for around 30 min to ensure all material melted and then poured into a graphite mould with a thickness of approximately 5 mm. To produce micron-sized powder, a Herzog HSM 100 vibratory mill with Tungsten Carbide (WC) vessel was used milling casted material pieces in batches of ~200 g running at 1400 rpm for 30 s. In addition, A RETSCH® Planetary Ball Mill PM 100 was used to mill the ingots down to nanosized powder. 20 g ingot were loaded together with stainless steel balls into a WC milling jar in an inert atmosphere (Ar). The ratio of milling ball, sample, and free space is 1/3: 1/3: 1/3 in volume. The powder was milled at 300 rmp with 2 min milling time and 1 min break to release the local heat, alternatively. The particle size distribution of the micron-sized powder was measured with a Malvern Mastersizer 2000, the D50 is around 5 μm, and a relatively broad range of particle sizes between 1 and 20 μm.

To consolidate the powder into ingots, Spark Plasma Sintering (Dr Sinter, SPS-825) was used. The powder was enfolded in graphite paper, loaded into a crucible (in an inert environment), and then cold-pressed using a manual hydraulic press at ~0.5 MPa. The cold-pressed pellet was then loaded in the SPS machine, pressure and temperature increased to 90 MPa and 850 °C (at 100 K/min heating rate), respectively. This temperature and pressure were held for a dwell time of 2 min. Furthermore, the temperature was reduced to 800 °C and pressure to 30 MPa. From then on, the pressure was released, and the pellets cooled naturally to room temperature.

2.2. Oxidation and microstructure analysis

The oxidation experiments were conducted using a TGA/DSC 1 (Mettler Toledo) on both powder and bulk samples. For isoconversion experiments, the powder samples were oxidised from room temperature to 1100 °C, with a constant heating rate of 5 °C/min in synthetic/dry air (5.0) with 50 ml/min purging rate. Isothermal experiments were carried out on bulk specimens, at temperatures from 250 °C to 600 °C for 24 h. Moreover, long-term oxidation experiments were conducted using an electric kiln SQ11 (KITTEC®) for 200 h in ambient air at 300 °C and 400 °C.

The oxidation residue was studied using Powder diffraction x-ray spectroscopy (XRD) for powder samples and X-ray photoelectron spectroscopy (XPS) on bulk samples. The XRD powder diffraction spectroscopy was carried out using a D8 Advance XRD instrument (from BRUKER). The instrument was set at 40 kV and 40 mA with a Cu X-ray tube. A continuous diffraction pattern was collected in locked coupled scan mode with a step size of 0.02° in the 2θ range of 10–80°. Moreover, the phases were qualitatively identified using the Bruker software EVA using the ICDD PDF-2 database.

Table 2
List of samples, nominal composition, and maximum isoconversion weight gain.

Sample ID[a]	Nominal composition	Powder - Total Weight gain [%]
$MnSi_{1.75}$	$MnSi_{1.75}$	12.673
Mo0.5_α	$Mn_{1.005}Mo_{0.005}Si_{1.75}$	8.878
Mo2_β	$Mn_{0.97}Mo_{0.02}Si_{1.75}$	5.32
Ge0.5_α	$Mn_{1.01}Si_{1.745}Ge_{0.005}$	5.671
Ge1_β	$Mn_{0.99}Si_{1.74}Ge_{0.01}$	7.726
Mo0.5- Ge0.5_β	$Mn_{0.985}Mo_{0.005}Si_{1.745}Ge_{0.005}$	19.116
Mo0.5- Ge1_γ	$Mn_{0.995}Mo_{0.005}Si_{1.74}Ge_{0.01}$	5.543
Mo2- Ge0.5_γ	$Mn_{0.98}Mo_{0.02}Si_{1.745}Ge_{0.005}$	7.86
Mo2- Ge2_α	$Mn_{0.99}Mo_{0.02}Si_{1.73}Ge_{0.02}$	6.663
Mo0.5-a	$Mn_{1.0095}Mo_{0.005}Si_{1.75}$	7.762
Mo1-a	$Mn_{1.0090}Mo_{0.010}Si_{1.75}$	8.352
Mo1.5-a	$Mn_{1.0085}Mo_{0.015}Si_{1.75}$	8.658
Mo0.5-b	$Mn_{1.0105}Mo_{0.005}Si_{1.75}$	7.455
Mo1-b	$Mn_{1.0100}Mo_{0.010}Si_{1.75}$	8.038
Mo1.5-b	$Mn_{1.0095}Mo_{0.015}Si_{1.75}$	8.075
Mo0.5-c	$Mn_{1.0115}Mo_{0.005}Si_{1.75}$	8.649
Mo1-c	$Mn_{1.0110}Mo_{0.010}Si_{1.75}$	8.531
Mo1.5-c	$Mn_{1.0105}Mo_{0.015}Si_{1.75}$	8.221

[a]Greek letters and a to c denote distinct Mn concentration in HMS before doping.

The XPS surface analysis was conducted using a Kratos Axis Ultra^{DLD} spectrometer with Al Kα X-ray monochromatic source (hν=1486.6 eV, at 10 A and 15 kV). The survey and high-resolution spectra were collected using step sizes of 1 eV and 0.1 eV, respectively. Similarly, the pass-energies used were 160 eV (survey spectra) and 40 eV (high-resolution core-level spectra). The spectra analysis was conducted using CasaXPS software, while the binding energy axis was calibrated using adventitious carbon (C-C) C 1 s photoemission peak centred at 284.8 eV. Further details and analysis of the XPS data are detailed in [2]. On bulk specimen, the microstructure images were taken using SEM (JEOL 772), the microscope was operated at a working distance of 10 mm and accelerating voltage of 15 kV. Based on backscattered images, the oxide phase composition was detected using an energy dispersive X-ray spectrometer (EDS) detector and analysed through line scan, spot analysis, and phase mapping using TEAM™ software (EDAX®-AMETEK®).

3. Results

3.1. Microstructure of the alloys

Among the alloys in Table 2, Mo2_β and Mo2- Ge2_α were selected to investigate the phase composition of the respective compounds, the selection is based on that is doped on the Mn site only while the other on both Mn and Si sites. Fig. 1 shows bulk $Mn_{0.97}Mo_{0.02}Si_{1.75}$ and $Mn_{0.99}Mo_{0.02}Si_{1.73}Ge_{0.02}$ SEM - backscattered electron (BE) micrographs, and Table 1 contains the EDS elemental compositions of spots shown on (a) and (b), respectively. The micrographs show that both compounds are multiphase alloys. $Mn_{0.97}Mo_{0.02}Si_{1.75}$ is composed of a heterogeneous mixture of $MnSi_{1.75}$, MnSi, and a ternary Mn-Mo-Si phase. HMS is the majority phase and is composed of relatively bigger grains, while the other two phases are minor especially MnSi, which is mainly found at the $MnSi_{1.75}$ grain boundaries. As discussed in our recent publication on oxidation of HMS [2], increasing the dopant (Al or Ge on the Si site) concentration from 0.5 at% towards 2 at% substantially increased the amount of MnSi striation in the compound. However, as shown by Fig. 1 substituting Mn with Mo relatively reduced the concentration of the one-to-one Mn-Si phase in the bulk.

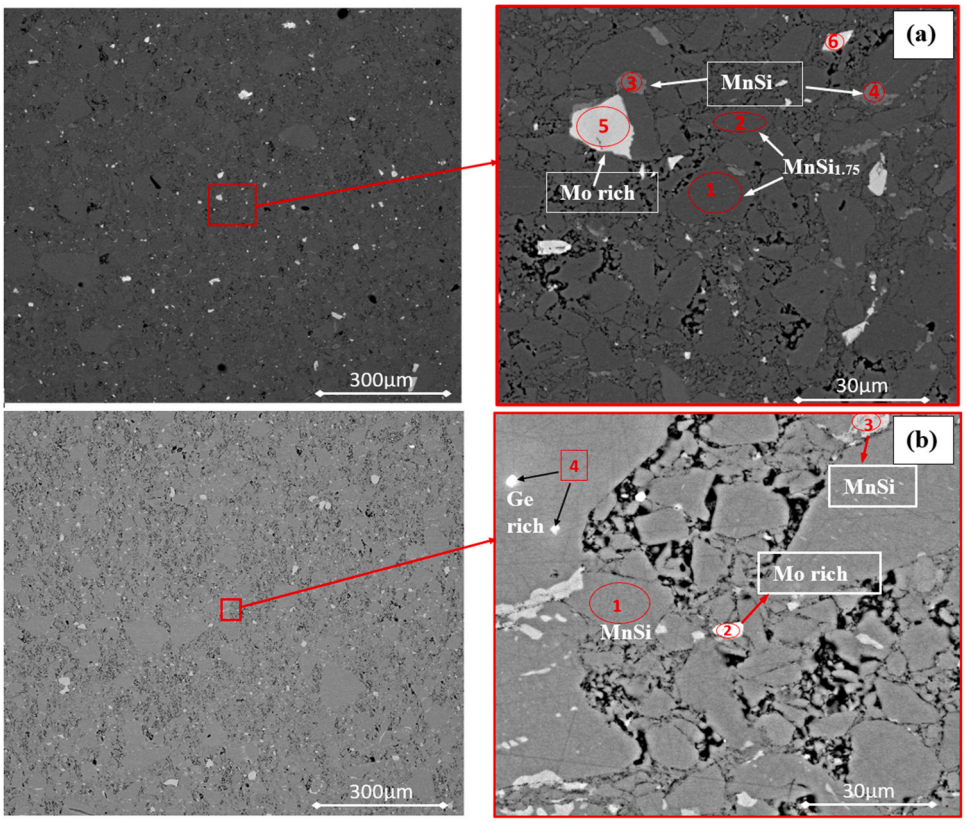

Fig. 1. As consolidated alloys' EDS spot analysis (see nominal composition in Table 1), (a) $Mn_{0.97}Mo_{0.02}Si_{1.75}$, (b) $Mn_{0.99}Mo_{0.02}Si_{1.73}Ge_{0.02}$.

Similarly, doping on both Mn and Si sites exhibited non-homogeneous microstructures, mostly composed of the $MnSi_{1.75}$, MnSi, and two ternary phases (Mn-Mo-Si and Mn-Si-Ge). As a general remark, it is evident that with doping on both sites the MnSi phase increases and the grains are bigger than doping on Mn Site only. There is no quaternary phase (Mn-Mo-Si-Ge) achieved, as a result of non-resolved "Ge" and "Mo" dopants as thoroughly described by J.S. Graff [13].

3.2. Isoconversion

The isoconversion was conducted on powder samples from 25 °C - 1100 °C with a 5 °C/min constant heating rate. Fig. 2 represents (a) three batches (α, β, and γ) of HMS with Ge and Mo dopants on the Si and Mn sites, respectively, and (b) batches (a, b and c) of HMS with Mo as dopant on the Mn site only. The zoomed images (upper right conners) show the oxidation at low temperatures (25 °C - 450 °C). All powders lost weight below 100 °C which is linked to humidity evaporation, while significant weight gain(oxidation) begins between 200 °C - 300 °C. The oxidation onset temperature varies with the dopant(s) concentration, where the higher the dopant concentration, the lower the onset temperature. In addition, the HMS alloys with low dopant concentration are more robust to oxidation relative to high doped compounds Fig. 3(a). However, at high-temperature oxidation (up to 1100 °C), the alloys are more robust with high dopant concentration Fig. 3(b).

Based on the XRD spectrum Fig. 4, silica (SiO_2) is the dominant and stable oxide phase among other present oxide phases. This is witnessed through Differential Scanning Calorimetry (DSC) Fig. 4(b), where the silica scale crystalizes at 420 °C, 540 °C, and 960 °C to form alpha quartz, beta quartz, and beta tridymite, respectively. The alloys' oxidation kinetics remain steady till 900 °C for most of the samples Fig. 2(a), except for those with higher Ge impurities which the weight gain rate was steeper at around 600 °C associated with germanium oxidation. Meanwhile, manganese- and molybdenum-based oxides were also present, which could be noticed by the endothermic reaction at 665 °C in Fig. 2(a) and (b).

3.3. Isothermal oxidation

The isothermal oxidation experiments were conducted to investigate the effect of doping HMS (on the Mn and/or Si sites) based on the thermal oxidation kinetics from 250 °C to 600 °C. Fig. 5 shows (a) the final relative weight gain of HMS alloys (with different dopant concentrations) after 24 h of isothermal oxidation in dry air. The magnified plot in the upper left corner shows that the weight gain of most of the alloys is below 1 µg/mm^2 up until 450 °C. Though the doping effect is minimal at low temperatures, the trend indicates that increasing Mo or Ge concentration translates into an increase in weight gain during oxidation. The doping effect was more pronounced on alloys with doping on both Mn and Si sites, where varying doping concentrations from 0.5 at% to 2 at% increased around ten times the weight gain, even at low temperatures (<450 °C).

Fig. 6 are maps of weight gain data per unit area of, three among studied compounds with different dopant concentrations, (a) $Mn_{1.005}Mo_{0.005}Si_{1.75}$, (b) $Mn_{0.985}Mo_{0.005}Si_{1.745}Ge_{0.005}$ and (c) $Mn_{0.99}Mo_{0.02}Si_{1.73}Ge_{0.02}$. The data were recorded every hour during isothermal treatment at respective temperatures (250 °C - 600 °C), and as the compound in (c) had the most weight gain, (a) and (b) data were mapped on (c) scale for comparison purpose. The dopant effect is shown by the trend of weight gain over time. With both Mo and Ge doping (0.5 at% each), the oxidation rate is reduced relative to the compound with Mo doping only, however with increased dopant concentration (2 at% on both Mo and Ge), the weight gain is substantially increased by one order of magnitude especially at higher temperature.

From 250 °C to around 450 °C, the oxidation kinetics fit well both linear and logarithmic oxidation laws (oxidation rates per model

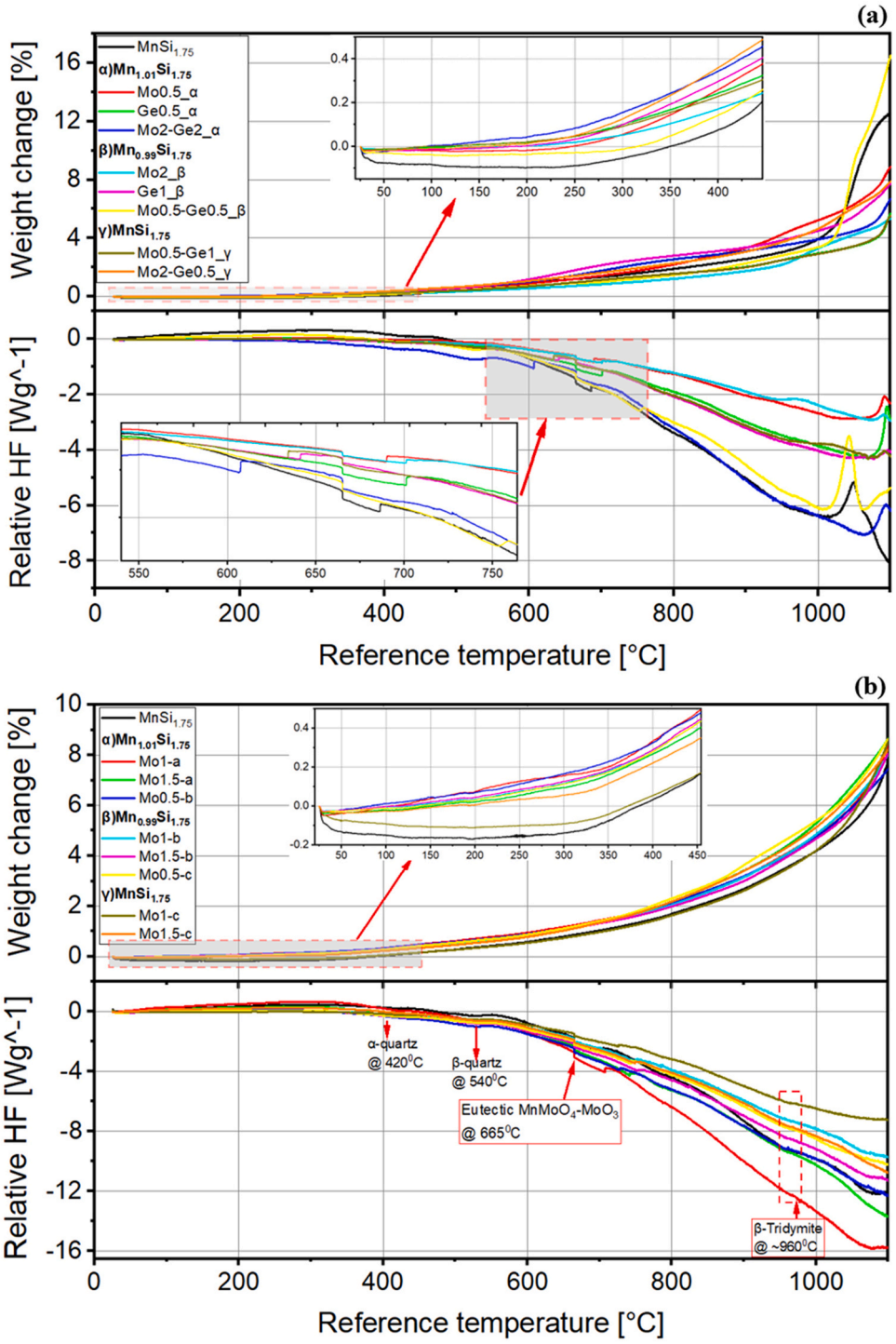

Fig. 2. TGA representation of HMS powder samples (a) Compounds with Ge and Mo dopants on the Si and Mn sites, respectively, (b) Only with Mo doping on the Mn site oxidized in Dry air from room temperature to 1100° C. Zoomed areas show oxidation at low temperatures 25 °C - 450 °C.

summarized in Table 3), however, as from the studies conducted on oxidation of Si [14,15], logarithmic law is considered the right model to represent the Si oxidation kinetics. Similarly, the logarithmic model was empirically found to better describe the HMS alloys oxidation in this study (mostly at 400 °C). That is simply because, Si is the major oxidation reactive element for all alloys and despite the well-known diffusion-controlled model (parabolic rate law), at low temperature, the oxidation reactions are much more reaction controlled than diffusion controlled.

On the other hand, Fig. 5(a) shows that at 600 °C for all alloys the weight gain course substantially deviated to a higher oxidation rate regime. The deviation is also shown for example on the TGA oxidation weight gain graph of Mo2-Ge2 Fig. 5(b), where the major factor is the weight gain at 600 °C where the oxidation followed a parabolic model. Therefore, in contrast to low temperature, HMS alloys above 500 °C oxidised parabolically. Table 3 tabulates the oxidation rates "kp" (approximated using Arrhenius model) of the studied alloys and addresses the composition effects on oxidation of the alloys (summarized in Table 3) as follows:

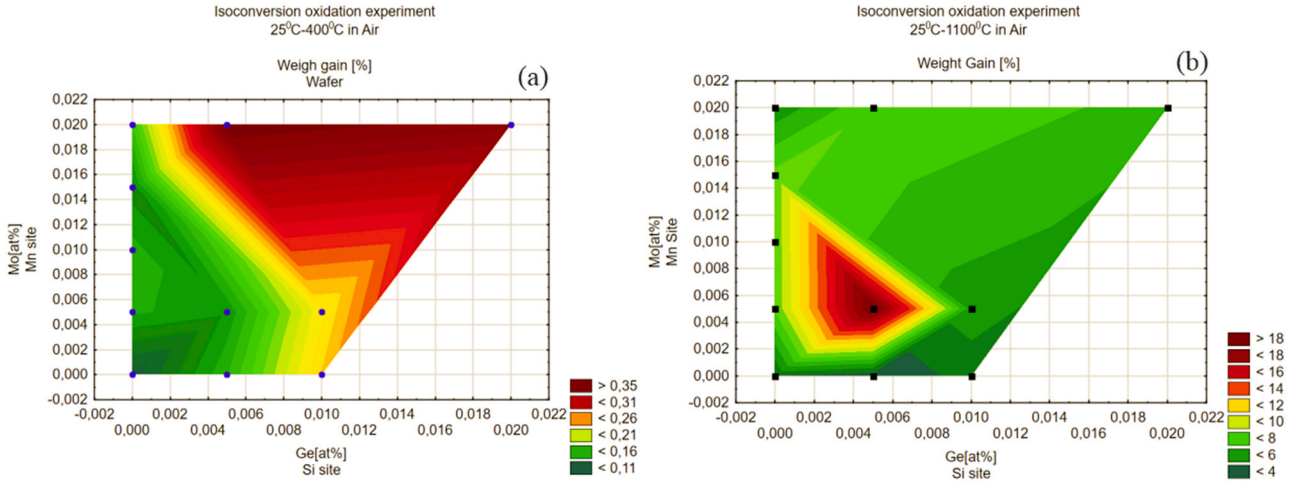

Fig. 3. Three-dimensional wafer map of the oxide weight gain after thermal oxidation in Dry air in the temperature range (a) 25 ℃ - 400 ℃ and (b) 25 ℃ - 1100 ℃. Round and square spots represent the plotted data position.

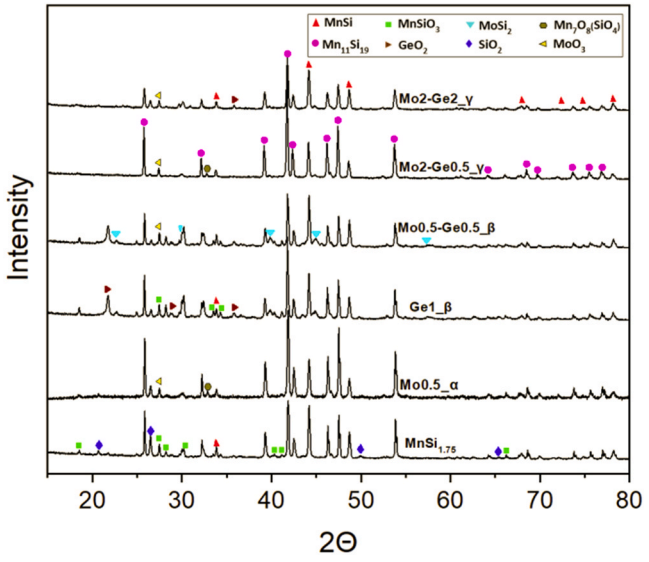

Fig. 4. X-ray powder diffraction spectrum showing the composition of the powder residue after oxidation at 1100 °C of the alloys marked by the samples ID as in Table 1.

a. For all alloys at low temperatures (250 ℃ – 350 ℃), the thermogravimetric behaviour is similar, with oxidation rates of around 0.12 μg/mm^2. Moreover, the weight gain during oxidation follows the linear kinetics model or logarithmic model (especially for alloys with low dopant concentration). Empirically, the weight gain data following linear or logarithmic rate laws cannot be distinguished numerically (kp) or by looking at the TGA curves. However, as will be discussed in later sections, logarithmic rates have numerically lower kp values than linear rates. For example, in Table 3, $Mn_{1.005}Mo_{0.005}Si_{1.75}$ if both at 250 ℃ and 300 ℃ are fitted linearly, the growth rate at the higher temperature is lower than at lower temperature. Therefore, at 300 ℃ the oxidation kinetics follows logarithmic model.
b. Between 350 ℃ - 450 °C, most of the alloys followed logarithmic model, especially at 400 ℃. Another common trend among all alloys is that the lower the dopant the more the alloys follow logarithmic law. The latter can be seen on alloys with Mo doping or Mo and Ge doped alloys, which means that it would take longer for compounds with higher Mo dopant to grow a protective scale than for those with less Mo concentration. However, at higher temperatures (≥ 450 ℃), the alloys oxidise following parabolic law and logarithmic low. Table 3 shows that the alloys with low dopant 0.5–1 at% follow parabolic law, while from and above 2 at% dopant concentration the alloys still follow logarithmic law.

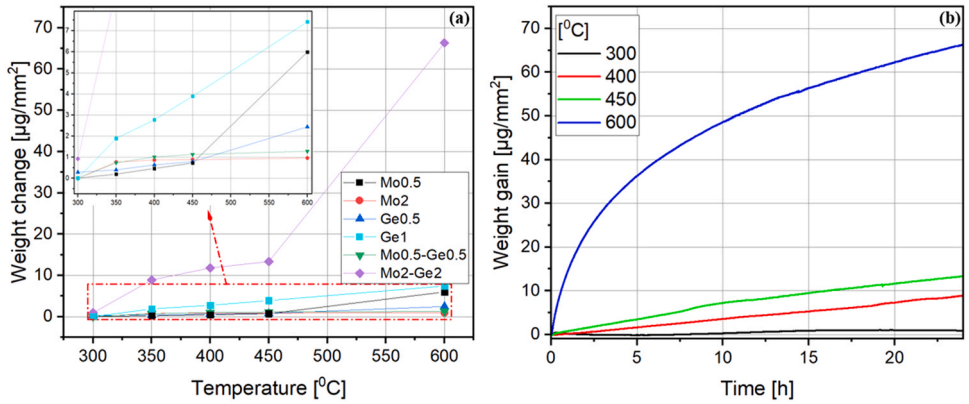

Fig. 5. Weight gain after isothermal TGA oxidation in synthetic air (5.0) for 24 h. (a) Comparison of different HMS alloys with different dopant concentrations (Mo dopant on the Mn site and Ge on the Si site) from the maximum weight gain at respective oxidation temperatures, (b) Isothermal TGA of Mo2-Ge2 at temperature from 300 °C to 600 ℃.

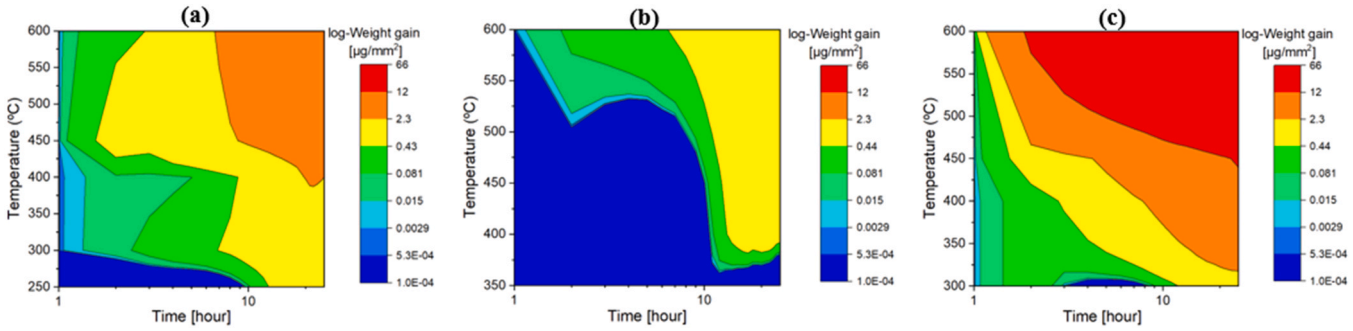

Fig. 6. Contour plot for the weight gain versus time at temperature from 250 °C - 600 °C. (a) $Mn_{1.005}Mo_{0.005}Si_{1.75}$, (b) $Mn_{0.985}Mo_{0.005}Si_{1.745}Ge_{0.005}$ and (c) $Mn_{0.99}Mo_{0.02}Si_{1.73}Ge_{0.02}$.

Table 3
Oxidation kinetics approximated by the Arrhenius model, the reaction rates are tabulated at specific temperatures and the model that the data fit symbolized by the superscript letter a to c.

Alloys	Weight gain - rate (kp) and law					
	250	300	350	400	450	600
$Mn_{1.005}Mo_{0.005}Si_{1.75}$	0.13[a]	0.08[b]	–	0.7[c]	0.9[c]	2.5[c]
$Mn_{1.005}Mo_{0.02}Si_{1.75}$	0.11[a]	–	0.12[a]	0.02[b]	0.46[b]	–
$MnSi_{1.74}Ge_{0.005}$	0.11[a]	–	0.114[a]	0.23[b]	2.91[c]	–
$MnSi_{1.74}Ge_{0.01}$[2]	–	–	–	0.07[b]	0.02[c]	0.2[c]
$Mn_{0.985}Mo_{0.005}Si_{1.745}Ge_{0.005}$	–	–	0.16[a]	–	0.2[c]	0.22[c]
$Mn_{0.99}Mo_{0.02}Si_{1.73}Ge_{0.02}$	–	0.12[a]	1[a]	0.4[b]	0.6[b]	12[c]

[a] Linear law[µg/mm2],
[b] Logarithmic law[µg/mm2],
[c] Parabolic law [µg2/mm4].

c. Finally, around 600 °C, the growth rate follows parabolic law for all compounds.

3.4. Oxide scale micrographs and composition

3.4.1. XPS analysis

To acquire XPS data, samples were flooded with low-energy electrons to compensate for the charging effects. Fig. 7 shows the Mn 2p, Si 2p, and O 1 s high-resolution spectra core lines. For Mn 2p spectra, peaks at ~ 642 eV and ~ 654 eV were ascribed to the 3/2 and 1/2 spin-orbit splitting components, respectively, and are indicative of the Mn-oxide phases. However, the $Mn_{1.005}Mo_{0.02}Si_{1.75}$ (at 400 °C) showed the presence of another component at low binding energy as indicated by an arrow in Fig. 7. Compared to the Mn $2p_{3/2}$ (638.8 eV) for manganese silicide, this component appears at high binding energy. In case of a sample that consists of phases with different electrical properties, charge compensation may lead to differential charging. As a result, the relative position of the peaks coming from different phases may shift. To confirm if this chemical shift is due to differential charging, data was collected without and with flooded low energy electrons for charge compensation. After calibration of the binding energy axis using adventitious carbon (284.8 eV), the oxide component lines up. However, this is not the case for the silicide component.

Stable manganese oxide grows at different oxidation states (Mn^{2+}, Mn^{3+}, and Mn^{4+}), exhibiting many multiplet splitting [16]. It is, however, challenging to conduct a quantitative analysis due to the coinciding binging energies of the multiplet splitting structures [16,17]. However, manganese oxidation states can be identified from the Mn 2p peak features and the magnitude of the Mn3s peak splitting. The absence of the satellite feature on the higher binding energy side of the Mn $2p_{3/2}$ peak rules out the presence of MnO [16,18]. Mn 3 s peak splitting of ~5.5 eV (not shown here) evidence the presence of manganese as Mn^{3+}. The Si 2p XPS spectra for $Mn_{1.005}Mo_{0.02}Si_{1.75}$ (at 400 °C) Fig. 7, showed an intense peak (~103.7 eV) corresponding to Si^{4+} oxidation state and a small feature at the low binding energy core indicative of Si in the low-oxidation state(s) [19]. Similarly, the O 1 s spectra exhibited two features which components 1 and 2 are characteristic of Si-oxide and Mn-oxide, respectively [20]. The relative amount of Si-oxide to that of Mn-oxide increases with the oxidation temperature as evidenced in Fig. 7.

Furthermore, Fig. 8 shows that higher oxidation temperature promotes the formation of SiO_2 phase. Sample $Mn_{1.005}Mo_{0.02}Si_{1.75}$ (at 400 °C) showed the presence of Si_2O_3 and Si_2O phases apart from SiO_2. Nevertheless, the Si_2O phase is not present in sample $Mn_{0.99}Mo_{0.02}Si_{1.73}Ge_{0.02}$ (at 400 °C).(Fig. 9).

Analysis of Mo3d core level region evidenced the presence of two phases, MoO_3 and MoO_2 [21]. At higher oxidation temperatures, the only phase observed is MoO_3. Fig. 10 shows the presence of the GeO_2

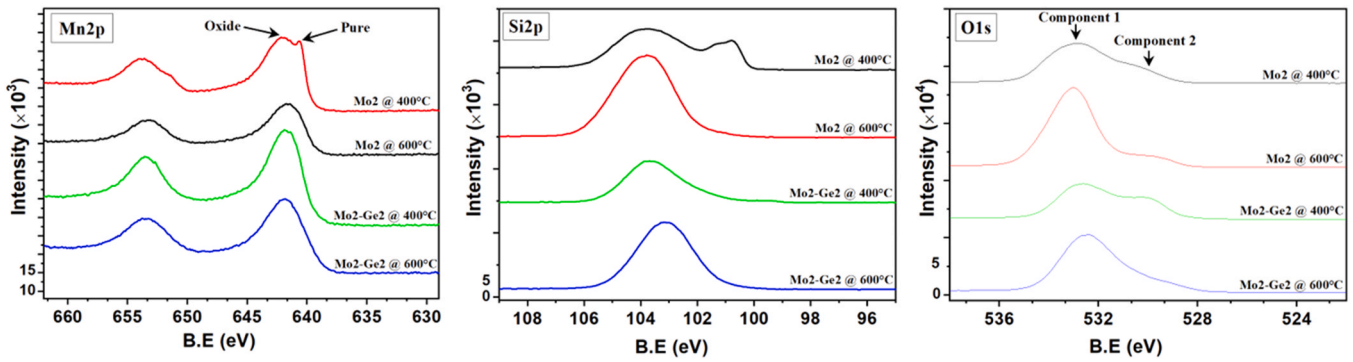

Fig. 7. X-ray photoemission spectra of the Mn 2p, Si 2p and O 1 s core-level regions.

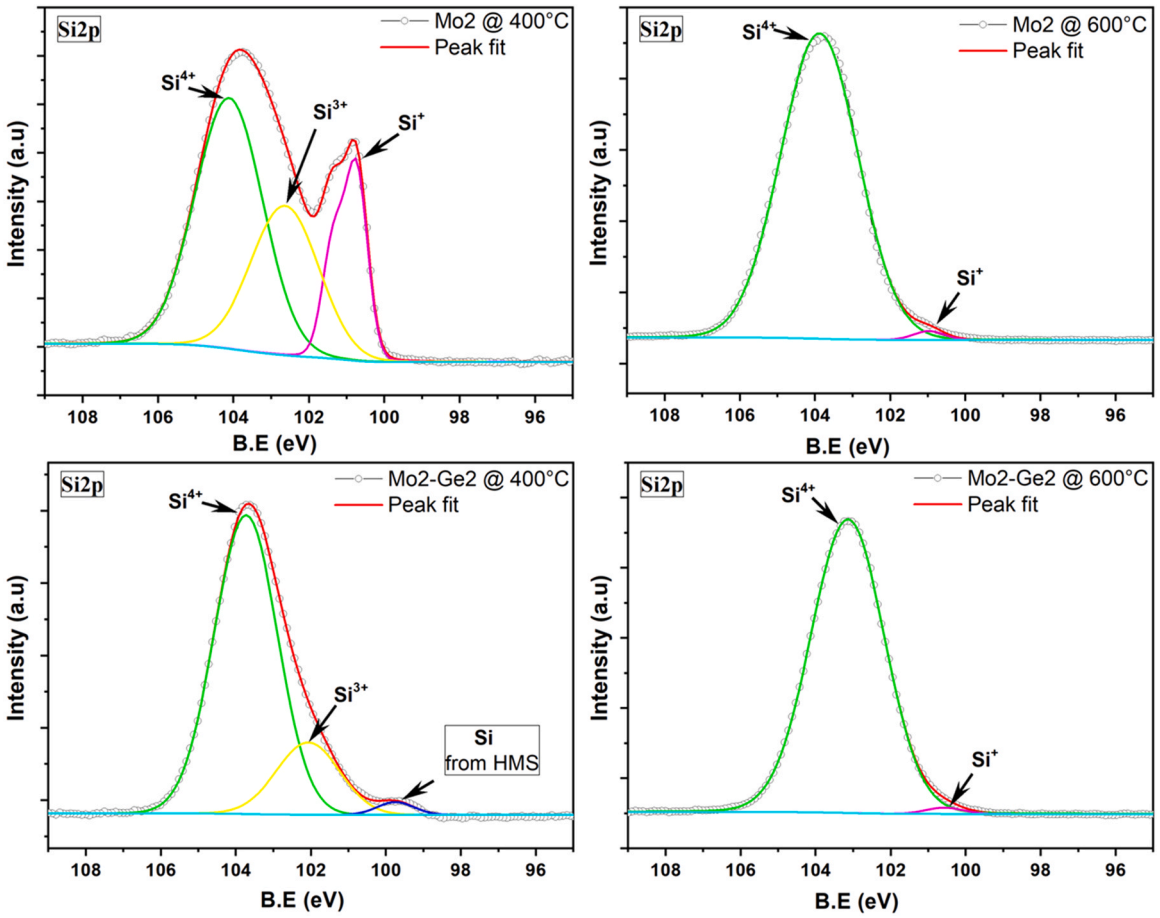

Fig. 8. X-ray photoemission spectra of the Si 2p core level region with peak fitting results.

phase in the Ge-doped samples [22]. However, at lower oxidation temperature (sample $Mn_{0.99}Mo_{0.02}Si_{1.73}Ge_{0.02}$ at 400 °C), another component at the lower binding energy side is present that is assigned to the elemental germanium.

3.4.2. SEM-EDS analysis

HMS alloys are robust to oxidation especially at low temperatures and short exposure to air, therefore, long-term exposure is key to enabling a microscopic visual analysis of the oxide scale. Figs. 11 and 12 present the SEM-EDS micrographs and phase maps of $Mn_{1.0095}Mo_{0.005}Si_{1.75}$ oxidation in air for 200 h at 300 °C and 400 °C, respectively. At 300 °C, a 150 nm non-uniform and coarse oxide layer can be seen. Much of the scale is SiO_2 as shown by the EDS phase maps, however, the lack of the other oxide species is attributed to the low detection level of the EDS detector. XPS as a more effective technique revealed the presence of Mn- oxides and Mo-based oxides (or Ge-based oxides for alloys with Ge dopant). Moreover, Fig. 11 shows that the oxide is thicker (around 250 nm) at the grain boundaries and thinner at the surface of the grains. This lack of scale uniformity at the alloy surface is due to the low phase homogeneity that leads to the presence of a conglomerate of oxides, especially at the grain boundaries. Fig. 12 on the other hand, shows that at 400 °C the oxide scale is more compact and thicker than at 300 °C. The oxide thickness is around 270 nm and is similarly composed mainly of SiO_2.

4. Discussion

4.1. The oxidation kinetic regimes

HMS alloys follow different oxidation models at respective temperatures as stated in the result section above, therefore it makes it difficult to experimentally approximate the energies of formation (for the alloys). Moreover, the alloys are robust to oxidation that in case of isothermal test carried out at short dwell time (24 h), it is difficult to accurately obtain reliable oxidation reaction rate using ideal cases Wagner theory since it does not consider some complicating factors including effects of impurities [23]. It is in that regard that, a new representation was adopted to discuss the mixed rate of oxidation per temperature as shown in Table 3. The technique used in this study employed the notion of Time-Temperature-Transform (TTT) diagram, to draw an oxidation map based on the thermogravimetric weight gain per unit area data of the actual alloys Fig. 6. The contour lines plots are not frequently used to interpret the oxidation kinetics of alloys. However, in this article, we adopted contour plots to recreate the oxidation weight gain profiles by projecting the elevations on the y-axis and distance on the x-axis (of the cartesian coordinate system) as in [24]. From the weight gain and oxidation rate profiles, the TTT diagram can be drawn in a simplified diagram, as in Fig. 13. The green and red curves are drawn based on TGA weight gain data of $Mn_{0.99}Mo_{0.02}Si_{1.73}Ge_{0.02}$, they represent the isothermal oxidation onset time and an approximate of the oxidation offset time, respectively. Further analysis and discussions are based on where you would land on the map if you projected data of a different alloy (among the studied compounds).

The TTT diagram, Table 3, and Table 4 combined reveal that the oxidation occurs through 4 different kinetic regimes.

1. Below 250 °C (represented by dashed area), the weight gain after 24 h was little to none, implying that the alloys were resistant to oxidation at low temperatures.

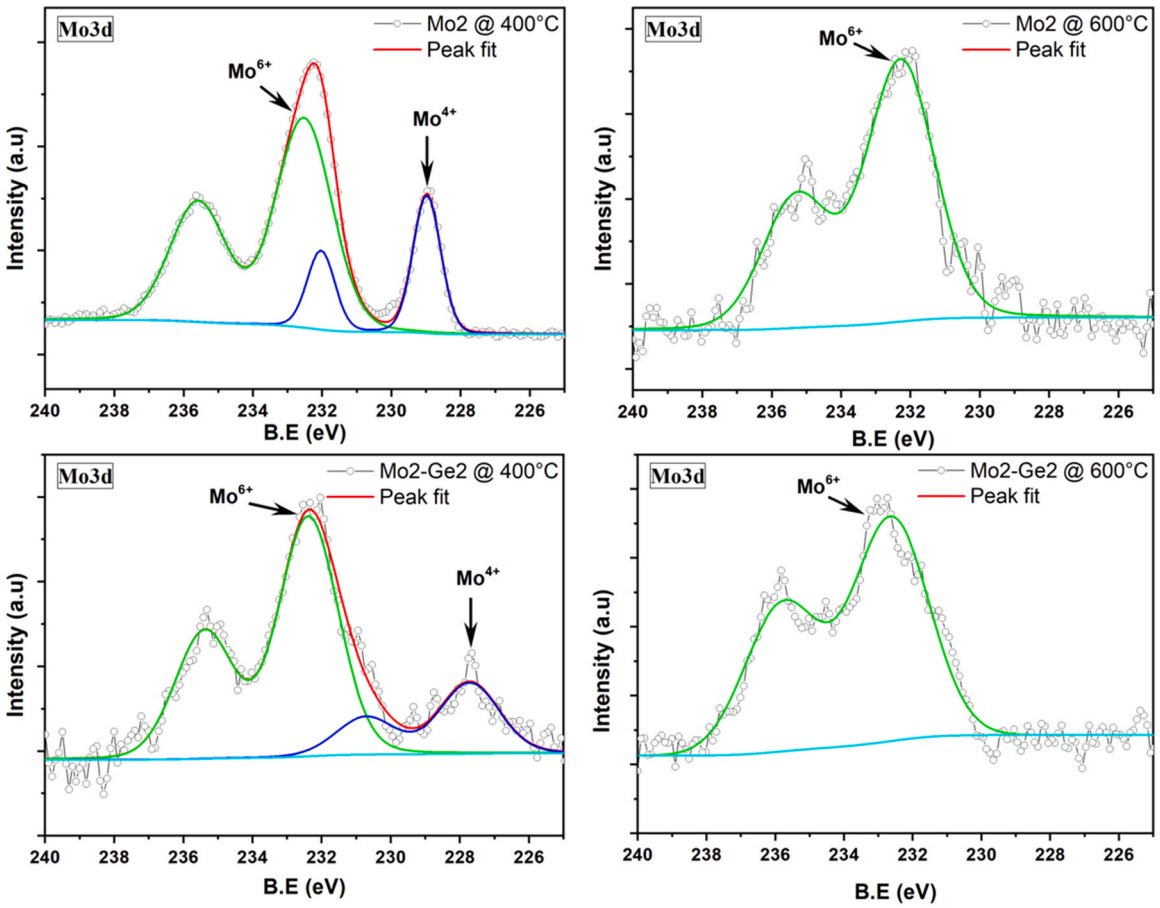

Fig. 9. X-ray photoemission spectra of the Mo 3d core level region with peak fitting results.

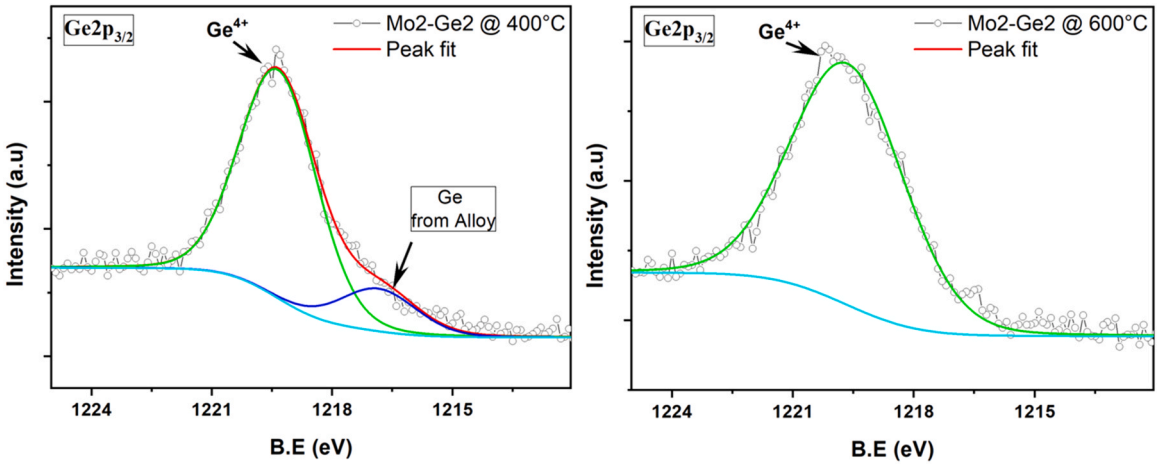

Fig. 10. X-ray photoemission spectra of the Ge 2p3/2 core level region with peak fitting results.

2. At temperature < 300 °C, the thermal gravimetric weight gain per unit area is low and fits the linear rate low (see the Byzantium colour area at the TTT diagram) as mentioned in Section 3.3. The linear rate law pertains to that, initially, the oxidant agent is adsorbed on the alloy surface at a constant rate(linear) until the whole surface is covered (monolayer) of adsorbate [25], therefore chemical reactions being the rate-determining process in this temperature range. By consulting Table 3, the linear regime extends up until 300 °C for alloys with high doping concentration and 350 °C for alloys with less doping. The same pattern is followed even at temperature > 400 °C, though, the gas adsorbate is quite fast and short (less than 1 h). The fast chemisorbed oxidant species at the oxide-gas interface, attract cations from the thin oxide scale to grow further the scale, though leaving hole defects in the old oxide phase. The latter creates cation defects gradient at the alloy-oxide phase that leads to consumption/transport of cations from the alloy across the alloy-oxide interface. At this point the scale is still too thin (hundreds of Angstroms ~1000) [26] and follows a logarithmic rate law (represented by the light and dark blue of the TTT diagram) for compounds with 2 at% dopant, while with less dopant the respective compounds fall

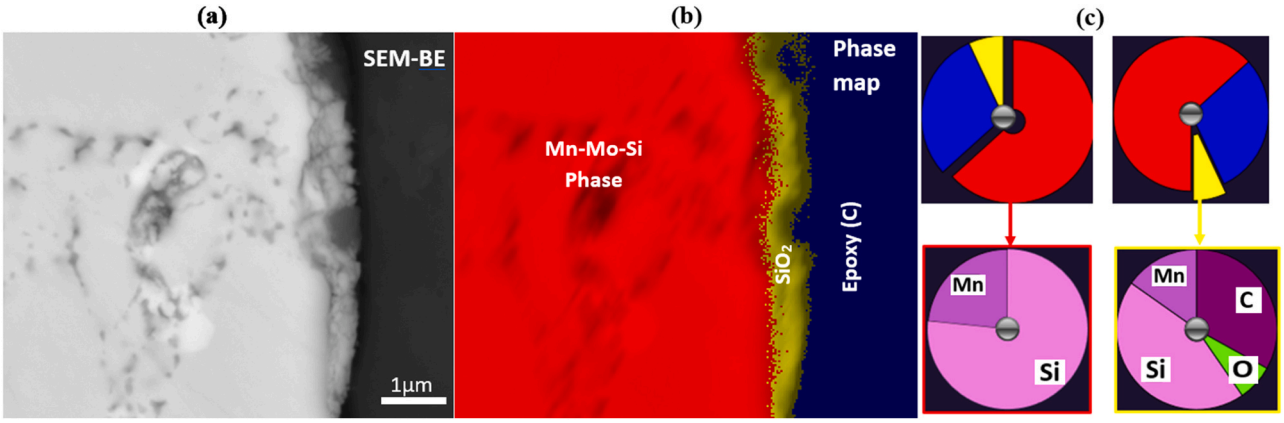

Fig. 11. SEM/EDS representation of $Mn_{1.0095}Mo_{0.005}Si_{1.75}$ oxidized at 300ºC for 200 h in ambient conditions. (a) Backscattered electron (BE) image, (b) EDS Phase map image showing the cross-section of the interface between alloy and oxide scale layers, and (c) elemental composition illustrative of phases in (b), red – alloy phase and yellow – oxide phase. (For interpretation of the references to colour in this figure legend, the reader is referred to the web version of this article.)

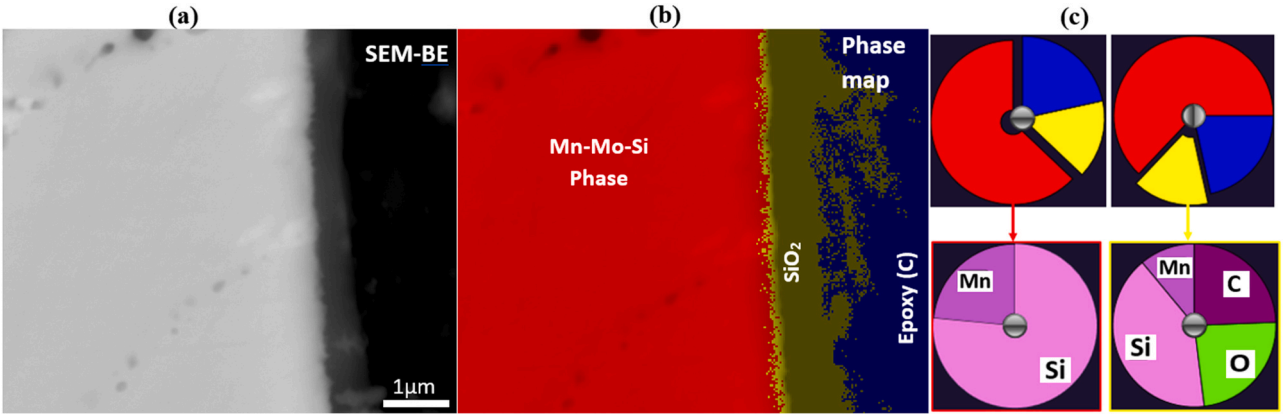

Fig. 12. SEM/EDS representation of $Mn_{1.0095}Mo_{0.005}Si_{1.75}$ oxidized at 400ºC for 200 h in ambient conditions. (a) Backscattered electron (BE) image, (b) EDS Phase map image showing the cross-section of the interface between alloy and oxide scale layers, and (c) elemental composition illustrative of phases in (b), red – alloy phase and yellow – oxide phase. (For interpretation of the references to colour in this figure legend, the reader is referred to the web version of this article.)

in the parabolic regime in this temperature range (the latter will be discussed at point 4 below).

3. The logarithmic law extends to higher temperatures of 500 °C and 600 °C for the respective compounds, though for a very short duration. The logarithmic regime is described as a state at which the reactive species adsorbed at the alloy surface (linearly), creates a diffusion of anions towards the alloy core and cations in the opposite direction that creates an electric field across the oxide-alloy interface [26]. As it can be seen from Fig. 13, in the first 24 h of isothermal experiments, logarithmic law would be the main rate law for the studied alloys especially at temperatures from ~300–400 °C. However, considering the long-term experiments at 300 °C and 400 °C, it was empirically concluded that the logarithmic regime reduces over time, as a result of reduced ion diffusion at the alloy-oxide interface.
4. Finally, the parabolic regime (represented by dark yellow colour), is characteristic of a protective layer mainly composed of SiO_2. Empirically the compounds with less dopant, fall in the parabolic regime earlier than with high dopant concentration. This is simply because with fewer impurities the alloys would follow a model clause to that of pure HMS, with which the oxidation is selective with "Si" being the preferential element. The parabolic regime extends towards 600 °C, and as the colour gets lighter meaning that the scale is less protective at higher temperatures, though the study was conducted up to 600 °C. In the parabolic regime, interdiffusion across the oxide scale is the rate-determining process.

To summarize, the TTT diagram in Fig. 13 in this case used as an oxidation map, shows that the compounds studied were isothermally resistant to oxidation below 250 °C in dry air. However, above that temperature, they follow different oxidation models (linear, logarithmic, and parabolic), depending on the isothermal temperature and/or the composition (impurities concentration). The more impurities the alloys contained, the longer the alloy oxidised following linear law, and the lesser the impurities (for example, HMS in an extreme case), the early the alloy oxidized parabolically, where the oxide is mainly SiO_2. It is worth noting that non-protective oxide below the green curve connotes that there is no or non-substantial oxidation reaction in that temperature range. Nonetheless, non-protective oxide above the red curve conveys a threat to the stability of the alloys.

4.2. *Mechanisms of oxidation*

The individual constituents of the $Mn_{x-\alpha}$ Mo_{α} $Si_{y-\beta}$ Ge_{β} alloys have got a certain affinity to oxygen which tends to create a mixture of oxides, therefore the need to protect the alloy from all elements to be involved. Originally the alloys model was designed with oxidation resistance taken into capital consideration. As illustrated in [2], at the beginning Si is the preferential element involved in oxidation forming SiO_2 oxide, and HMS should theoretically be able to provide sufficient flux of Si until a compact SiO_2 layer is formed. In case, Si concentration reduces below the minimum concentration at the alloy-oxide interface, other reactive

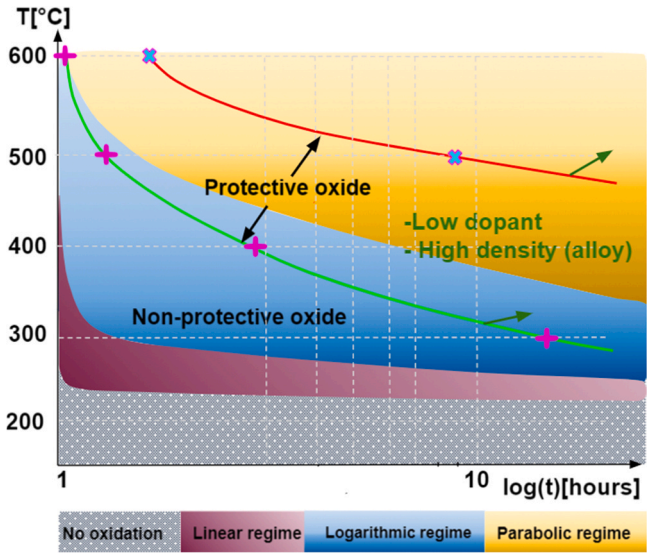

Fig. 13. The TTT diagram for isothermal oxidation of HMS with Mo and/or Ge as dopant(s). The green curve presents the process(oxidation) starts and the red curve - the process end. Green arrows point in the direct the curves are shifted towards relative to dopants concentration and density of the alloys. (For interpretation of the references to colour in this figure legend, the reader is referred to the web version of this article.)

Table 4
Classification scheme of the oxidation of the studies HMS alloys.

Class	Temperature range	Oxidation reaction	Rate governing factor	Oxide stability (Empirical)
1	< 250 °C	No signification reaction, hard to adhere to the alloy surface	The alloy robustness to oxidation	–
2	250–350 °C	Oxide scale is adherent to the alloy surface, significant weight gain starts after around 7 – 10 h of exposure, and fits a linear model	Chemical reaction (gas adsorption) at the alloy surface	1. Stable at low temperature 2. Stable over time[a]
3	400 °C < T < < 600 °C	Fast (1–2 h) gas adsorption (usually logarithmically), followed by a thickening of the oxide, mainly SiO_2 parabolic growth and protective.	Wagner diffusion-controlled or lattice diffusion of electrons/ions	1. Metastable for short[b] exposure 2. Stable over time
4	600 °C	Fast interdiffusion across the scale, and oxide volatility at higher temperatures (>700 °C)	Interdiffusion across the alloy-oxide interface, and oxide volatility	1. Stable for short exposure 2. Long-term should be investigated

[a] Long-term stand for 200 h;
[b] Short-term stand for 24 h

elements would be involved in oxidation. However, the coexisting Si, Mo, and Ge oxides mixture overlay in layers of the respective oxides, with the oxide with the higher solubility on the top (that being MoO_3, GeO_2, and SiO_2 at the alloy interface).

The above scenario is true for a homogeneous/single-phase alloy, but in case of multiphase or porous alloys, the oxidation mechanisms deviate from the ideal situation. The alloy studied being multiphase alloys, Fig. 14 is a schematic representation of the oxide growth mechanisms of $Mn_{x-\alpha}\,Mo_{\alpha}Si_{\,y-\beta}\,Ge_{\beta}$. The map is composed of 4 stages, starting from the original alloy composition (at the alloy surface – left on the figure) and progresses over time through stage 4, which is the final oxide layer studied using different surface characterization techniques (SEM-EDS and XPS) employed in this study.

Stage 2 of Fig. 14 shows the melt cast compound before oxidation, the composition of the alloys is as presented by the alloy's micrograph (Section 3.1) for further details. From the 3rd stage onward, it is evident that the alloys' oxidation mechanisms were a result of the alloy matrix structure and impurities' solubility. Therefore, the oxide growth on the alloy surface is governed by several oxidation processes. For HMS rich phase, the process follows the classic binary alloy oxidation theory, where Si is selectively reactive to oxidation and leaves a Si depleted phase with a composition close to MnSi at the alloy-oxide interface, where Wagner chemical diffusion (the theory of diffusion in solid oxides is also discussed by C.A.C. Sequeira [27]) is the rate defining factor.

On the other hand, based on the XRD results Fig. 4, two manganese silicates were detected as braunite (Mn_7SiO_{12}) and pyroxmangite ($MnSiO_3$). Moreover, Fig. 2(a) and (b) shows an endothermic reaction at 665 °C which is interpreted as the formation of a eutectic Mn-Mo oxide (33 wt% $MnMoO_4$ and 67 wt% MnO_3). The reaction occurrence is due to MnO_3, $MnMoO_4$, and Mn_2O_3 solid oxides mixture as by the Mn-Mo-O ternary phase diagram Fig. A1 [28] and discussed by K. Ivanov [29].

Above 1000 °C a sudden weight gain is noticed, early for less doped compounds (as Mo0.5-Ge0.5_β and $MnSi_{1.75}$). The exothermic reaction is represented by Eq. (1), and can also be seen in the MnO-SiO_2-O_2 computed phase diagram (using FactSage) in p(O_2)= 21% atm [30].

$$\frac{2}{3}Mn_7SiO_{12} + 4SiO_2 \;\rightarrow\; \frac{14}{3}MnSiO_3 + O_2 \tag{1}$$

$$Si + \;\; O_2 \;\rightarrow SiO_{2(S)} \tag{2}$$

Since none of the silicates was detected with XPS, the two would be attributed to being internal oxides or located at the alloy-oxide interface. It is difficult to know the exact mechanisms of formation of the two compounds, however, there are two possibilities. The first and most relevant is that the oxidant ions diffuse through the already formed oxide to react with the "Si" depleted layer, therefore the inner oxygen anions diffusion being the rate-determining factor. The second is that, though the presence of silica as protective oxide, the reaction of the dopants with oxygen may have compromised the level of protectiveness and lead to the formation of Mn-based oxides as shown in Fig. 14(3). Consequently, the coexisting Mn oxides and SiO_2 form a manganese silicate Mn_7SiO_{12} [31] as by Eq. (3), and the latter would transform into $MnSiO_3$ (check phase diagram, Figure) and release oxygen anion as shown by Eq. (1). Nevertheless, in both cases, the thicker SiO_2 gets the more the inner alloy surface will be attained.

$$2Mn_2O_3 + Mn_3O_4 + SiO_2 \rightarrow Mn_7SiO_{12} \tag{3}$$

As represented by Fig. 1, the alloys contain some Mo and Ge rich phases ($MoSi_2$ and possibly $GeSi_2$, respectively). Both phases contribute to the oxidation of the alloy, though following slightly different mechanisms to the classic binary alloy oxidation scheme they would follow if they were pure phases state. Unlike the case of oxidation of $MoSi_2$ [32] or $GeSi_2$ [33] compounds, at low temperature, the growth of MoO_2, MoO_3, and/or GeO_2 is much dominated by the growth of SiO_2 Fig. 14(3), that a continuous silica layer formation would leave them at the oxide/gas interface. Several studies [34,35] were conducted on the oxidation of Mo and showed that above 500 °C the Mo-oxide volatility increases, and becomes linear above 650 °C. Moreover, K. Ivanov [29], found that superficial Mo- oxides are not stable at temperatures above 600 °C.

To summarise, the alloys studied were multiphase alloys, which had a negative effect on the oxidation mechanisms of the alloys. As described

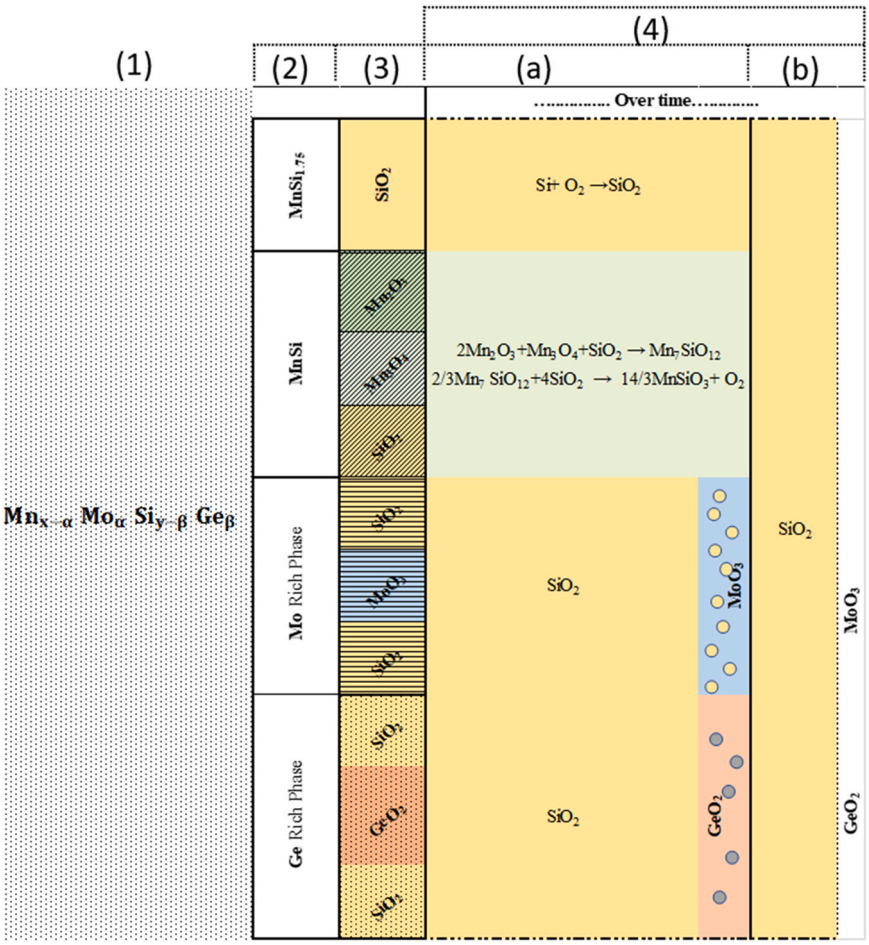

Fig. 14. Schematic representation of the evolution of the surface oxide layer of $Mn_{x-\alpha}$ Mo_α $Si_{y-\beta}$ Ge_β alloy in subsequent time steps from (1−4).

in a couple of paragraphs above, the overall performance of both short-term (24 h) and long-term (200 h) experiments showed that the compounds were resistant and resilient to oxidation. However, forasmuch as the dopants were involved in the early stage of the oxidation process, the thermoelectric performance (specifically the electrical conductivity) will much be affected because of reduced charge carrier concentration. It would highly be recommended to adapt/retune the synthesis method's parameters to achieve a more homogeneous compound, or possibly explore other possible synthesis methods rather than melt casting.

5. Conclusion

The oxidation of $Mn_{x-\alpha}$ Mo_α $Si_{y-\beta}$ Ge_β alloys are studied in the temperature range of 250–600 °C in synthetic air (5.0) for 24 h (for all alloys) and 200 h (for selected alloys). The study shows that the kinetic model of oxidation, varies from linear to parabolic at temperature around 300 °C and above. This is due to increased oxidation rate that originates from reaction to the oxidant agent of almost all elements that comprise the alloy. At low temperature (< 300 °C), chemical reactions at the alloy surface are the reaction rate-controlling factor in this temperature range. While at temperatures higher than 450 °C, diffusion through the oxide layer is the rate-determining factor, where SiO_2 is the main/dominant oxide phase. In addition, long-term experiments showed that the layer is protective with only 150 nm thick oxide at 300 °C and 250 nm thickness at 400 °C after 200 h. Therefore, revealing the potential of HMS alloys in the medium temperature range for thermoelectric application. Finally, based on the short-term (24 h) exposure experiments, all the alloys' constituents were involved in oxidation, which is unwanted. Though, this study did not determine how charge carrier density was affected by the alloy's oxidation, it is important to note that there is a level of materials consumption due to oxidation and take it into consideration during alloys' modelling stage. At temperatures lower than 400 °C, the alloys are resistant to oxidation even at longer thermal exposure, revealing the potential of HMS alloys in the medium temperature range for thermoelectric application.

CRediT authorship contribution statement

Antoine de Padoue Shyikira: Conceptualization, Methodology, Investigation, Validation, Formal analysis, Writing – original draft preparation, Writing – reviewing and Editing, Project administration. **Naureen Akhtar:** Methodology, Investigation, Validation, Formal analysis, Writing – original draft and Reviewing. **Gunstein Skomedal:** Grant writing and application, Conceptualization, Methodology, Supervision, Reviewing and Editing. **Peter Hugh Middleton:** Supervision, Reviewing and Editing.

Declaration of Competing Interest

The authors declare that they have no known competing financial interests or personal relationships that could have appeared to influence the work reported in this paper.

Data availability

Data used in this manuscript will be made available by the corresponding author upon reasonable request.

Acknowledgment

The authors would like to acknowledge the contribution of Elkem ASA, Sintef, and the University of Oslo (UiO) as partners in the TESil project. The contribution extends from material synthesis, pellet consolidation, and transport properties tests. Moreover, the authors would like to appreciate Ingvild Thue Jensen for her tremendous help in conducting the XPS tests. Finally, we acknowledge financial support from the Research Council of Norway (Project No 269326).

Appendix

See appendix Fig. A1 and Fig. A2.

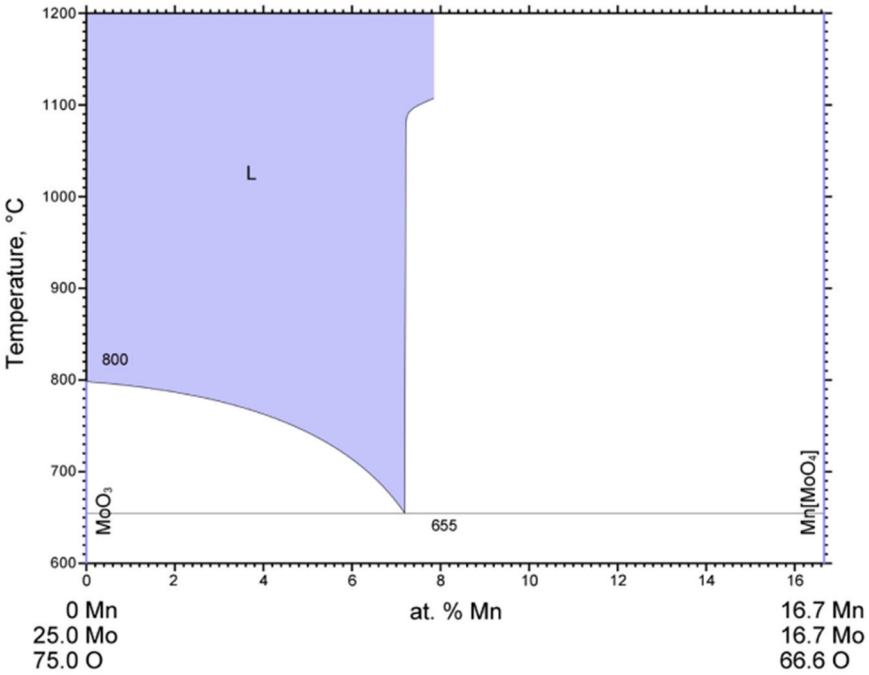

Fig. A-1. Mn-Mo-O Phase diagram [36].

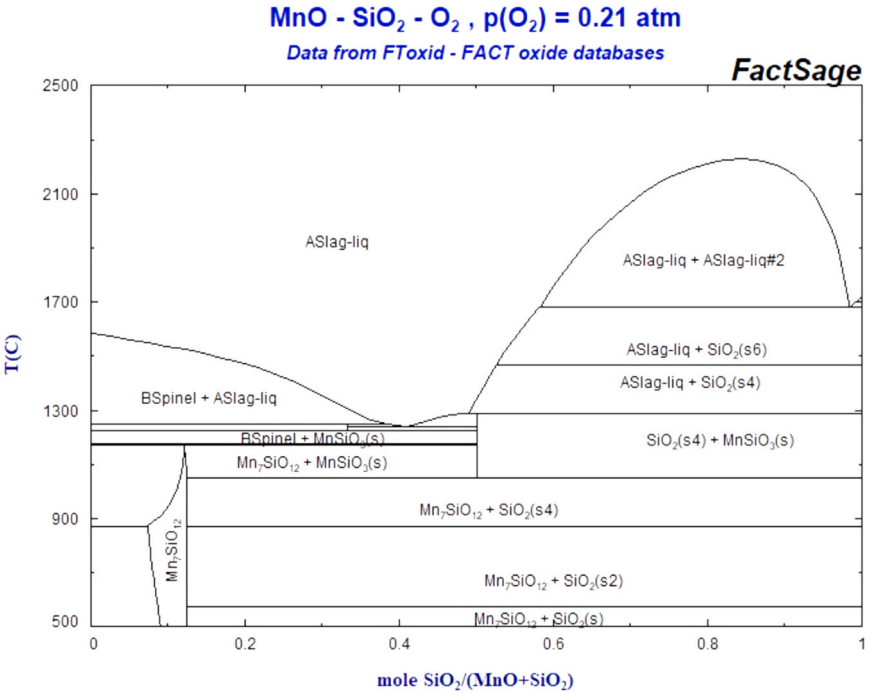

Fig. A-2. MnO-SiO_2-O_2 Phase diagram in P(O2) = 0.21 atm [30].

References

[1] D.P. Whittle, J. Stringer, Improvement in high temperature oxidation resistance by additions of reactive elements or oxide dispersions, Philos. Trans. R. Soc. Lond. 295 (1980) 309–329.

[2] Antoine de Padoue Shyikira, Naureen Akhtar, Gustein Skomedal, Tor Oskar Sætre, Peter Hugh Middleton, High temperature oxidation of higher manganese silicides (p), Corros. Sci. 185 (2021), 109327, https://doi.org/10.1016/j.corsci.2021.109327.

[3] Y. Miyazaki, 2.15. Higher manganese silicides, in Thermoelectric Energy Conversion, Woodhead Publishing, Sawston, 2021, pp. 374–387.

[4] I. Aoyama, M.I. Fedorov, V.K. Zaitsev, F. Solomkin, Yu, I.S. Eremin, A. Samunin, Yu, M. Mukoujima, S. Sano, T. Tsuji, Effect of Ge doping on micromorphology of MnSi in MnSi1.7 and on their thermoelectric transport properties, Jpn. J. Appl. Phys. 44 (12) (2005) 8562–8570.

[5] Yuzuru Miyazaki, Haruki Hamada, Hiroki Nagai, Kei Hayashi, Crystal structure and thermoelectric properties of lightly substituted higher manganese silicides, Materials 11 (6) (2018) 926.

[6] E.I. Suvorova, V.V. Klechkovskaya, Precipitates of MnSi cubic phases in tetragonal Mn4Si7 crystal, Crystallogr. Rep. 58 (6) (2013) 854–861.

[7] Quansheng Guo, Wenhao Zhang, Zihang Liu, Xiuwei Fu, Sylvain Le Tonquesse, Naoki Sato, Hyoung-Won Son, Kiyoshi Shimamura, David Berthebaud*, Takao Mori, Thermoelectric performance of Cr doped and Cr–Fe double-doped higher manganese silicides with adjusted carrier concentration and significant electron–phonon interaction, ACS Appl. Mater. Interfaces 13 (7) (2021) 8574–8583.

[8] Guo Liu, Qingmei Lu, Xin Zhang, Jiuxing Zhang, Yongjun Shi, In situ synthesis and thermoelectric properties of cr-doped higher manganese silicides, J. Electron. Mater. 41 (6) (2012) 1450–1455.

[9] H. Nagai, H. Hamada, K. Hayashi, Y. Miyazaki, Effects of cobalt substitution on crystal structure and thermoelectric properties of melt-grown higher manganese silicides, J. Electron. Mater. 48 (4) (2019) 1902–1908.

[10] P. Kofstad, Changes of Oxide Properties Through Doping, in High Temperature Corrosion, Elsevier Applied Science Publishers Ltd., London - Newyork, 1988, pp. 345–346.

[11] D. Naumenko, B.A. Pint, W.J. Quadakkers, Current thoughts on reactive element effects in alumina-forming systems: in memory of John Stringer (no), Oxid. Met. 86 (2016) 1–43, https://doi.org/10.1007/s11085-016-9625-0.

[12] P.Y. Hou, J. Stringer, The effect of reactive element additions on the selective oxidation, growth and adhesion of chromia scales, Mater. Sci. Eng. A 202 (1) (1995) 1–10.

[13] Joachim S. Graff, Raphael Schuler, Xin Song, Gustavo Castillo-Hernandez, Gunstein Skomedal, Erik Enebakk, Daniel Nilsen Wright, Marit Stange, Johannes de Boor, Ole Martin, Løvvik, Matthias Schrade, Fabrication of a silicide thermoelectric module employing fractional factorial design principles, J. Electron. Mater. 50 (2021) 4041–4049.

[14] Keunjoo Kim, Young Hee Lee, Myung Hwan An, Moon Suhk Suh, Chang Joo Youn, Kee Bang Lee, Hyung Jae Lee, Growth law of silicon oxides by dry oxidation, Semicond. Sci. Technol. 11 (7) (1996) 1059–1064.

[15] Zhijie Xu, Kevin M. Rosso, Stephen M. Bruemmer, A generalized mathematical framework for thermal oxidation kinetics, J. Chem. Phys. 135 (2) (2011), 024108.

[16] Zhi-Qiang Zou, Gao-Ming Shi, Li-Min Sun, Xiao-Yong Liu, Manganese nanoclusters and MnSi~1.7 nanowires formed on Si(110): a comparative x-ray photoelectron spectroscopy study, J. Appl. Phys. 113 (2013) 1–5.

[17] Mark C. Biesinger, Brad P. Payne, Andrew P. Grosvenor, Leo W.M. Lau, Andrea R. Gerson, Roger St.C. Smart, Resolving surface chemical states in XPS analysis of first row transition metals, oxides and hydroxides: Cr, Mn, Fe, Co and Ni, Appl. Surf. Sci. 257 (2011) 2717–2730.

[18] Huaxing Sun, Xiangdong Qin, Francisco Zaera, Chemical nature of the thin films that form on SiO2/Si(100) surfaces upon manganese deposition, J. Phys. Chem. Lett. 2 (20) (2011) 2525–2530.

[19] Annett Thogersen, Josephine H. Selj, Erik S. Marstein, Oxidation effects on graded porous silicon anti-reflection coatings, J. Electrochem. Soc. 159 (5) (2011) 1–7.

[20] Eugene S. Ilton, Jeffrey E. Post, Peter J. Heaney, Florence T. Ling, Sebastien N. Kerisit, XPS determination of Mn oxidation states in Mn (hydr)oxides, Appl. Surf. Sci. 366 (2016) 475–485.

[21] S. Al-Kandari, H. Al-Kandari, F. Al-Kharafi and A. Katrib, Surface electronic structure-catalytic activity correlation of partially reduced molybdenum oxide(s) for the isomerization of light alkenes and alkanes, Journal of Physics: Conference Series, vol. 100, 2008.

[22] Shingo Ogawa, Ryohei Asahara, Yuya Minoura, Hideki Sako, Naohiko Kawasaki, Ichiko Yamada, Takashi Miyamoto, Takuji Hosoi, Takayoshi Shimura, Heiji Watanabe, Insights into thermal diffusion of germanium and oxygen atoms in HfO2/GeO2/Ge gate stacks and their suppressed reaction with atomically thin AlOx interlayers, J. Appl. Phys. 118 (23) (2015), 235704.

[23] P. Kofstad, Comparison of Theory and Experiment. High Temperature Corrosion, Elsevier Applied Science Publishers Ltd., London - Newyork, 1988, p. 182.

[24] Britannica, T. Editors of Encyclopedia, Contour line, 26 10 2016. [Online]. Available: ⟨https://www.britannica.com/topic/contour-line⟩. [Accessed 06 04 2021].

[25] P. Kofstad, Phase Boundary Reactions. High Temperature Corrosion, Elsevier Applied Science Publishers Ltd., London - Newyork, 1988, pp. 261–262.

[26] Neil Birks, Gerald H. Meier, Fred S. Pettit, Mechanisms of oxidation. Introduction to the high temperature oxidation of metals, second edition.,, Cambridge University Press, Cambridge, 2006, pp. 39–74.

[27] Cesar A.C. Sequeira, Diffusion in Solid Oxides. High Temperature Corrosion Fundamentals and Engineering, Wiley, Hoboken - New Jersey, 2019, pp. 160–161.

[28] A. International, Manganese-Molybdenum-Oxygen Ternary Alloy Phase Diagram (based on 1973 Ziolkowski J.), ASM International, Ohio, 2011.

[29] K. Ivanov, P. Litcheva, P. Klissurski, T. Popov, Thermal stability of MnMoO4-MoO3 catalysts for methanol oxidation, J. Therm. Anal. 36 (1990) 1361–1368.

[30] FactSage, MnO-SiO2-O2 Phase diagram, ⟨https://www.crct.polymtl.ca/fact/phase_diagram.php?file=Mn-Si-O_MnO-SiO2_air.jpg&dir=FToxid⟩: FactSage.

[31] P. Palvadeau, P. Euzen, M. Queignec, J.P. Venien, Characterization of Mn7SiO12, a synthetic equivalent of “braunite” a natural mineral with various manganese sites, Mater. Res. Bull. 26 (9) (1991) 841–848.

[32] Neil Birks, Gerald H. Meier, Frederick S. Pettit, Oxidation of alloys. High Temperature Oxidation of Metals, Cambridge University Press, 2006, p. 132.

[33] H.K. Liou, P. Mei, U. Gennser, E.S. Yang, Effects of Ge concentration on SiGe oxidation behavior, Appl. Phys. Lett. 59 (1991) 1200–1202.

[34] E.A. Gulbransen, K.F. Andrew, F.A. Brassart, Oxidation of molybdenum 550C to 1700C, J. Electrochem. Soc. 110 (9) (1963) 952–959.

[35] M. Simnad, Aija Spilners, Kinetics and mechanism of the oxidation of molybdenum, J. Met. 7 (1955) 1011–1016.

[36] ASM International, Manganese-Molybdenum-Oxygen Ternary Alloy Phase Diagram, ASM International, Cleveland - Ohio, 2007.